3

PUMP-PROBE CATHODOLUMINESCENCE MICROSCOPY

We introduce pump-probe cathodoluminescence microscopy (PP-CL) as a novel technique to study ultrafast dynamics in materials using combined and synchronous excitation of electron and laser pulses. We present the design, implementation and characterization of the PP-CL setup. The light emitted by the sample, either PL, CL or a combination of both, is analyzed through spectral, time-correlated and lock-in measurements. We discuss the main considerations to take into account in PP-CL experiments and present the differences and similarities between PL and CL emission in terms of excitation volume, injection density, spectrum, quantum efficiency and carrier dynamics. The comparison is illustrated with experiments on GaAs and GaN substrates. Finally, we present the initial studies of carrier dynamics in Cu_2ZnSnS_4 using PP-CL.

3.1. INTRODUCTION

Cathodoluminescence (CL) microscopy is a powerful technique to resolve optical properties down to the nanometer scale, given the use of electrons as the excitation source. The spatial resolution of CL is limited by the electron beam size (~ nm), the interaction volume of the electron and carrier diffusion in the material. Recently, the emergence of ultrafast electron microscopy has enabled time-resolved CL studies, in which the emission and excitation dynamics of materials are investigated at the nanometer scale [72, 123, 124]. The time resolution of TR-CL is typically limited by the detection system (~ tens of ps). Instead, by combining optical and electron excitation in a pump-probe configuration we can achieve temporal resolutions down to the hundreds of fs regime, similar to optical pump-probe systems,

while taking advantage of the high spatial resolution given by the electron beam [96].

Pump-probe measurements, usually based on double-laser beam excitation, are routinely used across different research fields, including biochemistry, materials science and molecular physics [125–127]. In these experiments, a sample is excited with a pump beam (typically a laser pulse) and the resulting state is probed with a second beam (for example, another laser pulse), thus enabling the study of ultrafast processes. Even though fully optical pump-probe configurations are the most common ones, many different pump-probe schemes have been proposed, with changes either in one or both of the pump/probe beams [128, 129] or the detection scheme [130, 131]. In electron microscopy, pump-probe measurements using a laser-pump electron-probe configuration have been demonstrated [62, 75, 132]. A pump-probe based technique that has recently become popular is photon-induced near-field electron microscopy (PINEM), typically performed in a (scanning) transmission electron microscope, (S)TEM, which is based on the study of the electron energy loss and gain after interaction with an optically-excited nanostructure [87–89]. Other pump-probe-type works in a TEM include the study of the formation of chemical bonds [83], magnetization dynamics [84, 133] and optically-excited phonon modes [134, 135]. In scanning electron microscopes (SEM), previous studies have investigated the recombination dynamics in semiconductors of optically-induced carriers by analyzing the variations in the secondary electron signal [75, 136, 137]. In all these cases the sample is excited by the laser pump, while the electrons act as a probe. The probe signals are thus transmitted electrons (used for real and Fourier-space imaging or EELS, among others) or secondary electrons, from which a real-space image is formed.

In this chapter, we discuss the implementation and characterization of the first pump-probe cathodoluminescence (PP-CL) setup. Similar to previous work, our setup consists of a dual-beam system, with both a pulsed electron and laser beam. In contrast to earlier work, the emission and excitation dynamics are investigated through the analysis of the emitted luminescence, either CL or photoluminescence (PL). Hence, our setup allows us to use the electron beam either as a pump, thus probing the effect with the laser, or as a probe, after pumping with the laser. We illustrate the use of PP-CL with initial investigations of CL enhancement on optically-excited Cu_2ZnSnS_4, in which the electron acts as a probe. In the next chapter (Chapter 4) we study electron-induced charge state transfer on diamond nitrogen-vacancy centers, in which the electron acts as the pump.

3.2. OVERVIEW OF THE PP-CL SETUP

Our pump-probe experiments rely on the use of an electron and laser beam, in which one (pump) brings the sample out of equilibrium and the other one (probe) records the new state of the material. Tuning the delay between pump and probe gives access to the dynamics of the induced effect. The process of pumping and probing is repeated over many cycles ($> 10^6$) in order to accumulate enough signal (stroboscopic mode) [43]. Hence, this method can only be used to study reversible

phenomena, given that the sample has to go back to a steady (unexcited) state before each cycle of pump-probe.

Our pump-probe CL setup integrates an SEM with an optical setup containing a femtosecond laser (Fig. 3.1). We use a Thermo Fisher Quanta 250 FEG SEM $(0.5 - 30\,keV)$, which has been modified to give optical access to the electron gun through a UV-transparent window. The femtosecond laser (Clark MXR) consists of a diode-pumped Yb-doped fiber oscillator/amplifier system, providing 250 fs pulses at an output wavelength of $\sim 1035\,nm$ and tunable repetition rate (200 kHz-25.19 MHz). The laser beam is directed towards an optical setup (harmonic generator, HG) containing a set of BBO crystals (Clark MXR) to obtain the 2nd, 3rd and 4th harmonics of the fundamental beam ($\lambda = 517, 345$ and $258\,nm$, respectively). Figure 3.2 shows an image of the HG setup with the corresponding beam paths for the different harmonics. The HG setup is built such that we can use different combinations of two harmonics simultaneously, thus offering a large flexibility in a pump-probe experiment.

The PP setup can be divided into three main parts: electron, light-injection, and collection paths. The electron path consists of the coupling of the 4th harmonic laser beam ($\lambda = 258\,nm$) to the electron gun to induce photoemission of electrons. A detailed description of the electron path and the photoemission process is provided in Chapter 2. The light-injection path refers to the set of optical components designed to direct the laser beam towards the SEM chamber and focus it on the sample. The collection path denotes the set of optics and detection systems that we use to analyze the luminescence from the sample (either PL or CL).

The SEM, the collection path and part of the electron path are mounted on an air suspension system (see Fig. 3.1a), meaning that they move freely to compensate for vibrations in the room. Instead, the rest of optical components, including the laser, is mounted on a non-floating optical table. We use two identical feedback systems (TEM-Messtechnik μ-Aligna) (for the electron and light-injection paths, respectively) to actively track the movement of the floating section and move the laser beam accordingly, such that the alignment between both sections is maintained. The feedback system is composed of a position-sensitive detector (PSD), mounted on the floating section, and two motorized mirror mounts, mounted along the non-floating part (either the electron or the light-injection path). All components are connected through a controller. We use a beam sampler to send a small fraction of the laser beam to the PSD, which tracks the motion of the SEM with respect to the laser beam, and the mechanical actuators are moved accordingly to compensate for it.

We use an off-axis parabolic mirror (0.5 mm focal distance, parabola coefficient a=0.1 and 1.46π sr solid angle collection) placed above the sample both to focus the laser beam on the sample and to collect the luminescence (PL or CL). The mirror has a 600 μm diameter hole placed above the focal point through which electrons pass. A motorized stage (Delmic Redux) controls the position of the mirror in the direction parallel to the sample plane. We bring the sample to the focal point of the mirror by lifting the sample stage up to a working distance of around 14 mm (see
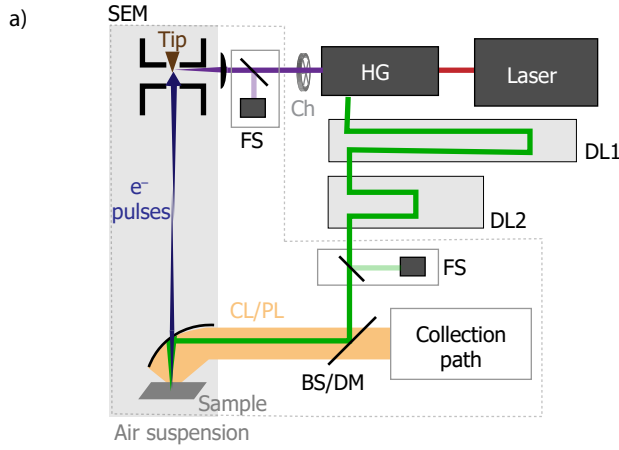
3

Figure 3.1: Pump-probe cathodoluminescence setup. Schematic (a) and photograph (b) of our PP-CL setup. The setup consists of the electron (purple), light-injection (green) and collection (orange) paths. The fundamental output ($\lambda = 1035\,\text{nm}$) of a femtosecond laser is converted to the 2nd, 3rd and 4th harmonics ($\lambda = 517, 345$ and $258\,\text{nm}$, respectively) in the harmonic generator (HG) setup. The 4th harmonic is focused on the electron cathode of the SEM to generate electron pulses. The 2nd or 3rd harmonics are directed towards the SEM chamber using either a beam splitter or dichroic mirror (BS, DM) to optically excite the sample. The delay between electron and light pulses is controlled using two delay lines (DL1 and DL2). The alignment between the air-suspended parts and the optical table is maintained using a feedback system (FS).
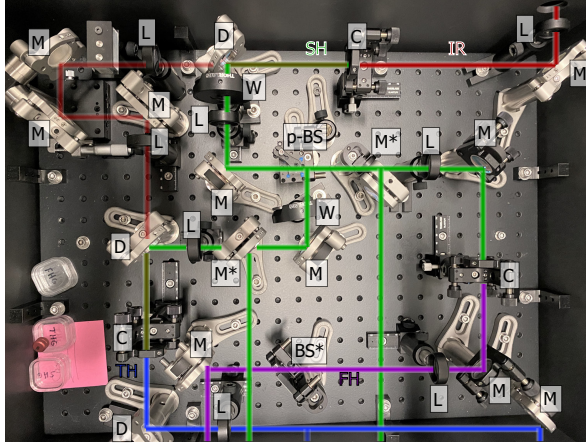
Figure 3.2: Photograph and beam path of the harmonic generator setup (Clark MXR). The fundamental laser beam (IR, $\lambda = 1035$ nm) is directed towards a set of BBO crystals to generate the 2nd (SH, $\lambda = 517$ nm), 3rd (TH, $\lambda = 345$ nm) and 4th (FH, $\lambda = 258$ nm) harmonics. This setup allows us to use different harmonics simultaneously. Abbreviations: mirror (M), lens (L), dichroic mirror (D), beam-splitter (BS), polarizing beam-splitter (p-BS) and BBO crystal (C). The asterisk denotes the components that can be flipped in and out of the beam path.

section 3.4.1). In the next sections we will describe in detal the coupling of the laser beam into the SEM chamber (light-injection path) and the detection and analysis of the emitted CL and PL (collection path).

3.3. LIGHT-INJECTION PATH

In our pump-probe setup, we excite the sample with both electron and laser pulses. Hence, we need to guide one of the harmonics of the fs laser towards the inside of the SEM chamber. In this thesis we use either the 2nd or 3rd harmonic beams ($\lambda = 517$ and 345 nm, respectively) to optically excite the sample. The 4th harmonic ($\lambda = 258$ nm) and fundamental laser beam ($\lambda = 1035$ nm) could also be used in the light-injection path by choosing appropriate optics. Figure 3.1 shows a schematic of the complete setup, in which the green line represents the light-injection path. The path is also designed to control the arrival time of the light pulses with respect to that of the electron pulses, which is essential in a pump-probe experiment. We use two free-space optical delay lines (DL1 and DL2 in the figure), consisting of a set of two mirrors (in the case of DL1) or a hollow retroreflector (Newport UBR2.5-5UV, for DL2) mounted on a mechanical stage. Moving the delay stage by 15 cm corresponds to a time delay of 1 ns, given the double path of the light along the stage.

The first delay line (DL1) is manually controlled and is used to adjust the zero-delay between electron and light pulses. We only align this stage at the start of an experiment, and it is kept fixed during a measurement. The operating electron energy of the SEM ($0.5 - 30$ keV) determines the electron arrival time on the sample.

Hence, we adjust DL1 in each experiment such that the arrival time of the laser on the sample matches the one from the electrons. As a reference, a 30 keV electron arrives 7.5 ns earlier to the sample than a 5 keV one, which corresponds to a delay stage movement of 1.125 m. This delay line is also used to compensate for the different path lengths of the harmonics inside the harmonic generator, resulting in variations in their arrival time (~ 1 ns). The total length of DL1 is 1.26 m.

In a pump-probe experiment, we tune the delay between electrons and light by moving the second delay line (DL2). We use a motorized linear stage (Newport M-IMS600BPP, and motion controller Newport ESP301-1G), with total range of 60 cm (4 ns), minimum step size of 1.25 μm (8.3 fs) and precision of 0.65 μm (4 fs). The stage movement is controlled using a script developed for the Odemis software (Delmic), such that its movement is integrated with the data acquisition. In an experiment we typically choose the center of this delay line to correspond to the zero delay between electrons and light, meaning that we can scan in a −2 to 2 ns range (with sign defined depending on the arrival time of the laser with respect to the electron). The temporal alignment of electron and laser beams on the sample is discussed in section 3.6.

After DL2, the laser beam is directed towards the SEM chamber using an 8:92 pellicle beam splitter (Thorlabs BP208) or a dichroic mirror optimized for either the 2nd or the 3rd harmonic (Semrock Di02-R532-25x36 and Di01-R355-25x36, respectively). The position and angle of the beam splitter or dichroic mirror is controlled by a kinematic mount and a linear stage, thus allowing us to precisely align the laser with respect to the parabolic mirror. Finally, the light is focused on the sample using the parabolic mirror described in section 3.2. The alignment of the laser beam on the sample is discussed in section 3.5.

3.4. LUMINESCENCE (CL/PL) COLLECTION PATH

After excitation with an electron or laser beam (or both), the luminescence is collected by the parabolic mirror (described in section 3.2). The resulting luminescence beam is collimated and has a size determined by the mirror dimensions (23 mm × 11 mm) [33, 138]. The luminescence is further directed outside of the SEM towards the detection path setup. A photograph of this optical setup is provided in Fig. 3.3, together with the corresponding schematic. We have four types of detection methods: angular, spectral, time-correlated and phase-locked. The optical components in the collection path are either on magnetic mounts or can be easily removed, such that we have full flexibility for different optical configurations, depending on the experiment. In the next sections we describe each of these detection schemes.

3.4.1. ANGULAR DETECTION WITH CCD CAMERA

The alignment of the parabolic mirror and sample height is performed by sending the CL light directly to a 2D back-illuminated thermoelectrically-cooled CCD silicon array (PI PIXIS 1024B, 1024x1024 pixels), operating at a temperature of −70 °C.
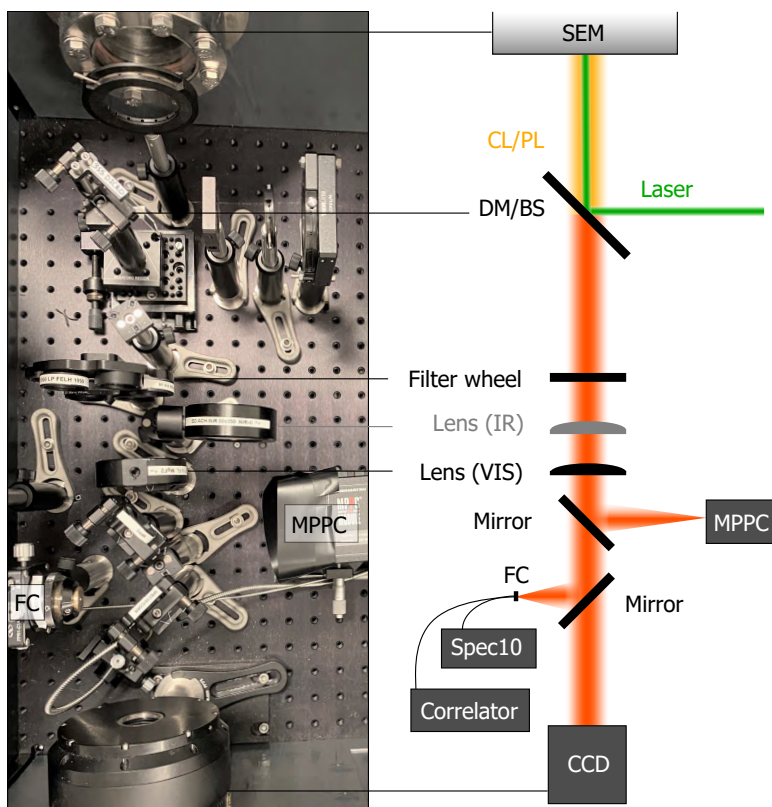
Figure 3.3: Luminescence (CL/PL) collection path. The light collected by the parabolic mirror is directed outside the SEM chamber for analysis. Different optical paths are available depending on the type of measurement: angular, spectroscopic, time-correlated or phase-locked. DM: dichroic mirror, BS: beam splitter, FC: fiber coupler, MPPC: multipixel phtoon counter.

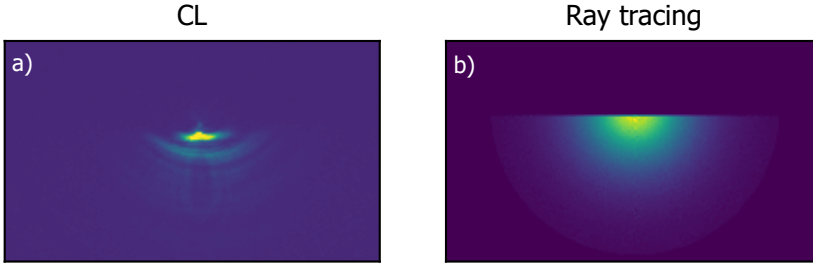CL   Ray tracing

Figure 3.4: CL alignment. (a) Pattern of the collimated CL beam on the CCD obtained when the parabolic mirror is aligned with respect to the sample. The image was obtained when exciting a GaN sample with a 5 keV continuous electron beam. (b) Ray tracing calculation of the image on the CCD obtained for a point source placed at the focal point of the parabolic mirror.

In this case we do not place any additional optical components in the detection path, such that we directly collect the collimated CL beam. An example of the image obtained on the CCD for an aligned parabolic mirror and sample is provided in Figure 3.4a, together with a ray tracing calculation of the pattern on the CCD obtained for a point source placed at the focal point of the mirror (Fig. 3.4b) [33, 139].

3.4.2. SPECTROSCOPY

Spectrally-resolved measurements in the visible range are performed by sending the emitted light through an achromatic lens ($f = 160$ mm, $d = 40$ mm) and a silver mirror (Thorlabs PF10-03-F01) to couple it to a multimode fiber with 550 μm core diameter (OZ Optics QMMJ-55-IRVIS-550/600-3AS-2). The fiber is mounted on a manually controlled 2D mechanical stage to optimize the coupling of light into the fiber in the plane perpendicular to the optical axis. The fiber guides the light to a spectrometer (PI Acton SP2300i) containing a liquid-nitrogen-cooled silicon CCD array (PI Spec-10 100F/LN, 1340x100 pixels), which reaches a temperature of -120 °C for enhanced signal-to-noise ratio (SNR).

The system response of the spectral measurements is characterized by measuring the spectrum of transition radiation (TR) of a single-crystal Al sample, similar to previous works [26, 41]. Figure 3.5a shows TR spectra obtained upon excitation with a 30 keV continuous electron beam (143.9 nA) when using a 150 gr/nm grating with 500 and 800 nm blaze (black and dark red, respectively). Fig. 3.5a also displays the calculated probability of photon emission per electron and wavelength bandwidth (green dashed curve), obtained using the formalism described in section IVC of ref. [25]. Using both curves we can extract the collection efficiency of our system ($\eta_{collection}$), defined as the number of counts detected per photon emitted by the sample. The results are shown in Fig. 3.5b for both gratings. The collection efficiency is not sample dependent, and can be used for any kind of CL and PL experiment, as long as we keep the same acquisition settings as in the TR measurements. Differences in the alignment of the parabolic mirror and fiber coupling can lead to
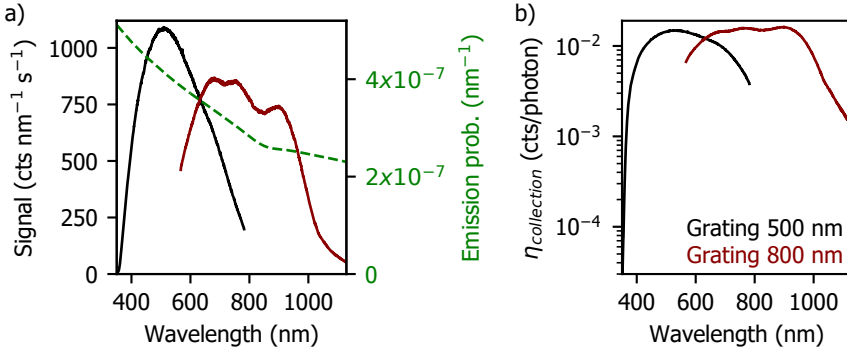
Figure 3.5: System response of spectral measurements. (a) Spectra of transition radiation of a single-crystal Al sample obtained under 30 keV electron excitation for a 150 gr/nm grating with 500 (black) and 800 nm (dark red) blaze. Right axis (green): Theoretical TR emission probability per electron. (b) Collection efficiency of the setup using both gratings of the spectrometer.

changes of ∼ 30 % in the collection efficiency [26].

3.4.3. TIME-CORRELATED MEASUREMENTS

We study the dynamics of laser or electron excitation and light emission using two types of time-correlated measurements: time-correlated single-photon counting (TCSPC) and second-order autocorrelation ($g^{(2)}(\tau)$) measurements.

TIME-CORRELATED SINGLE-PHOTON COUNTING

Time-correlated single-photon counting (TCSPC) measurements rely on the excitation of the sample with a pulsed beam (either electron or laser), and the subsequent analysis of the temporal statistics of the emitted light. We use the same optics (lens and mirror) as for the spectral measurements to couple the luminescence to a multimode fiber with 105 μm core diameter (Thorlabs FG105UCA). The fiber is connected to an external optical setup, mounted on a portable breadboard. A photograph of the setup is shown in Fig. 3.6a, together with a schematic of the optical path (in orange). The luminescence is initially attenuated using a tunable neutral density filter and can be spectrally filtered with an optical filter. Next, the light goes through a set of lenses (both $f = 7.5$ cm) to collimate and refocus it onto a single-photon avalanche photodiode (SPAD) (PicoQuant PDM Series). The SPAD has an active area of $100\,\mu m^2 \times 100\,\mu m^2$ and is mounted on a 3D mechanical stage for optimum alignment with respect to the light beam. The count rate is always kept below ∼ $10^6 s^{-1}$ to avoid damaging the detector. The entire correlator path is enclosed inside a light-tight enclosure in order to reduce background signal and protect the SPAD.

TCSPC measurements are performed by recording a histogram of the photon arrival time with respect to a reference signal (trigger), which is done using a time-correlator (PicoQuant PicoHarp 200). We direct part of the laser beam (usually the
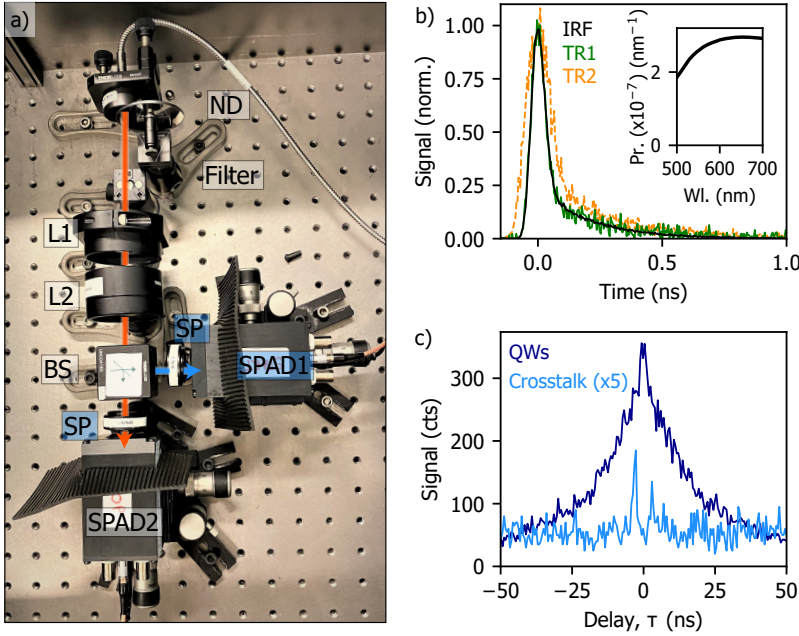
Figure 3.6: Time-correlated single-photon counting and autocorrelation $g^{(2)}(\tau)$ measurements. (a) Photograph of the optical setup used to perform time-correlated measurements. Here ND refers to a (tunable) neutral density filter, L1 and L2 are lenses, BS is a beam-splitter, SP is a short-pass filter and SPAD1 and SPAD2 are single-photon avalanche photodiodes. (b) Time resolution of the TCSPC system ($\sim 60\,\text{ps}$, black curve) obtained when sending the 2$^{\text{nd}}$ harmonic of the fs-laser towards the SPAD. The dispersion of the fiber is evaluated by measuring the time statistics of transition radiation on a single-crystal Au sample in the $620 \pm 5\,\text{nm}$ (TR1, green curve) and $532 - 670\,\text{nm}$ (TR2, orange curve) spectral ranges. Inset: theoretical calculation of photon emission probability of TR for a 30 keV electron pulse (Wl: wavelength). (c) CL $g^{(2)}(\tau)$ measurements of InGaN/GaN quantum wells (dark blue) and NV centers in diamond (light blue) obtained with a continuous 10 keV electron beam. The curve for the NV sample exhibits strong crosstalk.

2$^{\text{nd}}$ or 3$^{\text{rd}}$ harmonic) to a photodiode (PicoQuant TDA 200), which sends an electrical signal to the time-correlator, thus acting as a trigger. The time-correlator calculates the difference in arrival time between the trigger pulse and the electric pulse generated by the SPAD after detection of a CL/PL photon, thus resulting in a histogram of photon arrival time. In TCSPC measurements, only the first photon of each luminescence pulse is recorded. Hence, it is important to keep a low count rate to avoid an overestimation of the number of photons collected in the first time bins (pile-up effect), which would lead to the recording of artificially fast dynamics. This is solved by attenuating the emitted light such that, on average, less than one photon per pulse reaches the detectors.

The time resolution of the TCSPC setup is determined by the instrument response function (IRF) and dispersion in the optical fiber. We measure the IRF by directly sending the 2$^{\text{nd}}$ harmonic ($\lambda = 517\,\text{nm}$) of the fs-laser into the TCSPC setup,

as shown in Fig. 3.6b (black curve). Considering that the laser pulse width is negligible ($\sim 250\,\text{fs}$), we obtain an IRF of 60 ps (FWHM), which is determined by the precision of the correlator, SPAD and photodiode. In the case of a spectrally broad luminescence signal, we also need to account for dispersion in the optical fiber. In order to quantify this effect, we measured CL time traces of transition radiation (TR) on a single-crystal Au sample using different optical filters. Fig. 3.6b shows traces obtained when filtering the signal in the $620 \pm 5\,\text{nm}$ (TR1) and $532 - 670\,\text{nm}$ (TR2) spectral ranges (green and orange curves, respectively). In this case we used a 30 keV pulsed electron beam containing an average of 40 ± 15 and 80 ± 30 (green and orange curves, respectively) ($V_{\text{ext}} = 650\,\text{V}, C_1 = 1050\,\text{V}$, see Chapter 2). The inset shows the theoretical emission spectrum, calculated using the formalism from ref. [25]. TR emission can be assumed as instantaneous ($\sim 20\,\text{fs}$ [31]), hence the width of the time trace is determined by the IRF, dispersion of the fiber and electron pulse width ($\sim$ ps, see Chapter 2). We observe that the curve obtained when filtering the luminescence in the $620 \pm 5\,\text{nm}$ range resembles the one for the IRF obtained with the laser, thus suggesting that both dispersion in the fiber and electron pulse width are negligible. Instead, measuring luminescence in a broader range ($532 - 670\,\text{nm}$) results in a broader time trace, which we attribute to dispersion in the optical fiber. From the measurements we estimate a dispersion of $\sim 0.2\,\text{ps}\,\text{nm}^{-1}\,\text{m}^{-1}$, which is reasonable for a glass-type fiber. The temporal broadening due to dispersion in the fiber could be removed by having a completely free-space coupling system.

SECOND-ORDER AUTOCORRELATION ($g^{(2)}(\tau)$) MEASUREMENTS
To gain further insights in laser and electron excitation dynamics, we can study the CL and PL photon correlation statistics, which are measured using second-order autocorrelation ($g^{(2)}(\tau)$) measurements. Given a time-dependent luminescent intensity $I(t)$, $g^{(2)}(\tau)$ is defined as [140]

$$g^{(2)}(\tau) = \frac{\langle I(t)I(t+\tau)\rangle}{\langle I(t)\rangle^2} \, , \tag{3.1}$$

where the angle brackets denote the time average. Hence, in a $g^{(2)}(\tau)$ measurement we build a histogram of the number of coincidence events, defined as the detection of two photons, with respect to the time delay between them (τ). Our $g^{(2)}(\tau)$ experiments are performed using a Hanbury-Brown and Twiss geometry [141]. We use the same optical setup as for TCSPC measurements, with the difference that we now use two SPADs (1 and 2 in Fig. 3.6a, blue path). Both detectors are connected to the time-correlator. A 50:50 beam splitter is placed after the last lens, such that the CL/PL photons have equal probability of being detected by each SPAD. After detection of a photon by SPAD1 at a given time t_1, the time-correlator acts as a stopwatch until a photon is detected on SPAD2 (at a time t_2). A count is added on the histogram at a delay corresponding to $\tau = t_2 - t_1$. A $g^{(2)}(\tau)$ measurement is always symmetric, given that there is an equal probability of detecting a photon first on SPAD1 and then SPAD2 ($+\tau$) or viceversa ($-\tau$). An example of a $g^{(2)}(\tau)$ measurement in CL is shown in Fig. 3.6c (dark blue), performed when exciting In-GaN/GaN quantum wells with a continuous 10 keV electron beam. More details on

the spectrum of the sample and $g^{(2)}(\tau)$ measurements are shown in Chapter 5. In this example we used a 450 ± 40 nm bandpass filter.

A potential concern in $g^{(2)}(\tau)$ measurements is the phenomenon of crosstalk. After detection of a photon, SPADs can emit secondary photons, typically in the infrared spectral range (> 700 nm) [142]. In $g^{(2)}(\tau)$ measurements, the detection of this secondary photon by the second SPAD leads to the appearance of peaks at specific delays in the $g^{(2)}(\tau)$ curve. Figure 3.6c shows an example of this effect, obtained when exciting nitrogen-vacancy (NV) centers in diamond with a continuous 10 keV electron beam. The amplitude of the curve was multiplied by 5 for visibility purposes. The curve exhibits two peaks at delays corresponding to $\tau \approx \pm 2.8$ ns. Here we used a 650 ± 75 nm bandpass filter together with a 670 nm short-pass filter placed in front of each SPAD. The probability of having crosstalk can be reduced by further filtering out the longer wavelengths, as shown in Fig. 3.6c (dark blue). Hence, in this setup, $g^{(2)}(\tau)$ measurements are limited to wavelengths ranges below ~ 600 nm.

3.4.4. LOCK-IN DETECTION

The previously described detection systems are based on the direct collection and analysis of the emitted light. In pump-probe mesurements we have two signals: photoluminescence and cathodoluminescence, usually with very different magnitudes. This means that any spectrally or temporally-resolved measurement performed with the methods described above will be dominated by the largest signal. Hence, the analysis of the weaker signal becomes challenging, given that it can become buried in the noise of the larger signal. In our PP measurements, PL is typically several orders of magnitude larger than the CL signal, partially due to the larger PL spot area compared to the CL one, as will be discussed below (section 3.5.1). Moreover, when using the laser as a pump, a large excitation fluence is usually needed to achieve nonlinear regimes, thus further increasing the PL/CL ratio.

A method to extract the weaker signal (here, CL) is by decreasing the measurement bandwidth, such that noise is reduced, by means of lock-in detection. In this case, we focus the luminescence (CL/PL) on a thermoelectrically-cooled multi-pixel photon counter (MPPC module, Hamamatsu C14455-3050GA, 2836 pixels). The MPPC is connected to a lock-in amplifier (Stanford Research Systems RS830 DSP). Lock-in amplifiers work as phase-sensitive detectors, which can isolate small signals modulated at a known frequency and filter out other frequency components, thus improving the signal-to-noise ratio. This allows us to separate the desired signal from noise or background signal. In our experiments, we use an optical chopper (Thorlabs MC2000B-EC) to modulate the laser beam that we use to generate electron pulses (4th harmonic), typically at a few hundreds of Hz, thus resulting in a modulated CL emission. The chopper is also connected to the lock-in amplifier and serves as a reference signal. This mechanism allows us to isolate the CL signal from a large PL background, given the difference in CL and PL modulations.

In a pump-probe measurement we usually compare the magnitude of the probe
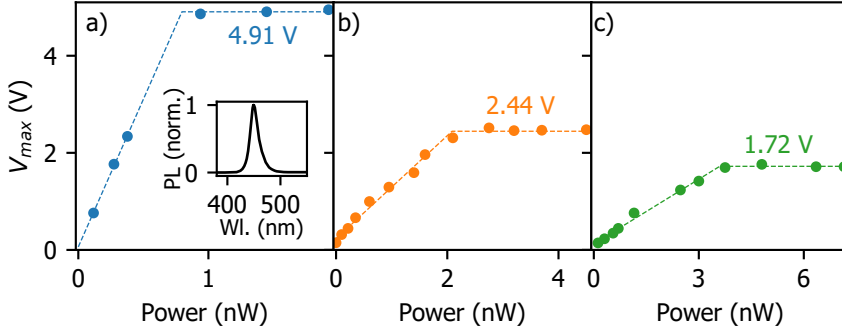
Figure 3.7: Response curve of the multi-pixel photon counter (MPPC) module. Dependence of the output voltage on the PL power incident on the MPPC at 1, 5.04 and 25.19 MHz repetition rates (a,b and c, respectively). The measurement was performed when exciting InGaN/GaN quantum wells with the 3rd harmonic of the laser. The inset in (a) shows the PL spectrum.

signal (either CL or PL) with and without pumping the sample (with laser or electrons, respectively). Hence, the detector (MPPC in our case) should have a low noise level so that it can detect small signals, in our case CL (< pJ), and a large dynamic range so that large PL signals do not saturate the detector, thus causing nonlinear behavior. Saturation of the MPPC during the experiment would result in artificially low signals in the pump-probe measurement compared to the reference (only CL or PL) one.

The output voltage of the MPPC as a function of incident power is shown in Figure 3.7 for different laser repetition rates. Here the input power is PL emission from InGaN/GaN quantum wells upon excitation with a $\lambda = 345$ nm laser beam (3rd harmonic). The PL spectrum is shown in the inset of Fig. 3.7a, and shows emission in the $400 - 450$ nm spectral range [41] (see also chapter 5). We chose to perform the characterization using PL emission, instead of directly sending the laser towards the MPPC, to mimic the conditions of an actual pump-probe experiment. The PL power was measured using a silicon photodiode (Thorlabs S120VC) placed along the PL path. Given the lower sensitivity of the photodiode compared to the MPPC, we placed a neutral density (ND2) filter in front of the MPPC to attenuate the incoming PL. The MPPC shows a linear response up to a certain power P_{max}, above which saturation is observed. The curves obtained at different repetition rates exhibit a different P_{max}, ranging from 3.6 nW at 25.19 MHz down to 0.8 nW at 1 MHz. We obtain a maximum output voltage of 4.98 V at 1 MHz, very close to the expected maximum output of the MPPC (5 V). Instead, the maximum voltage goes down to 2.44 and 1.72 V for 5.04 and 25.19 MHz, respectively. The dependence of the maximum power and output voltage on the repetition rate is attributed to the pixel recovery time. This analysis shows that in a pump-probe experiment it is crucial to ascertain that the output voltage of the signals (CL, PL and CL+PL) is sufficiently below the maximum output at the operating repetition rate.

3.5. LASER FOCUSING ON THE SAMPLE

We use the same parabolic mirror for luminescence collection (section 3.2) to focus the laser beam on the sample. This configuration allows us to focus the light down to a micrometer size spot without introducing additional components in the SEM chamber. Focusing with a parabolic mirror requires a precise alignment, given that any small misalignment can lead to aberrations, thus degrading the shape of the laser spot [143, 144]. Moreover, a precise spatial overlap of electrons and light is essential in pump-probe experiments. In this section we investigate the spot size of the laser on the sample and its alignment with respect to the electron beam.

In the experiments, we align the parabolic mirror by bringing the sample into focus while optimizing the CL pattern on a CCD camera, as explained in section 3.4.1. This guarantees maximum collection of the CL emitted light. The laser beam is then aligned on the sample by mechanically tuning the angle of the dichroic mirror or beam-splitter (see Fig. 3.9a) and position it with respect to the parabolic mirror. We can also use the feedback system to precisely tune the mirror actuators, thus yielding a higher angular and spatial control.

3.5.1. CHARACTERIZATION OF THE LASER FOCUS

Direct imaging of the laser spot on the sample plane is challenging due to its size (μm) and limited space in the SEM chamber. Instead, we can examine the change in secondary electron (SE) yield after optical excitation. Previous works have studied changes in SE emission in a pump-probe configuration ([136, 137]), from which the laser spot was imaged on the sample. For simplicity, here we rely on non-reversible changes in the SE contrast induced after repeated excitation with the laser (typically >10 s). Figure 3.8a shows an SE image of a 30 μm-thick GaN film on a sapphire substrate (PI-KEM, undoped n-type) after 10 s exposure with the 3rd harmonic laser beam ($\lambda = 345$ nm, 1.7 mW average power at 5.04 MHz). The scan was taken using a 5 keV electron beam with 380 pA electron current and 10 μs pixel integration time. We observe a centered elongated spot with a higher SE yield, which we attribute to the laser-exposed area. This is further confirmed by tracking the movement of this spot as we misalign the laser beam with respect to the sample, as will be explained below. The mechanism behind the change in SE signal upon laser excitation is unknown. We use a laser fluence (~ 0.4 mJ cm^{-2}) well below the reported damage threshold of GaN under UV fs-laser excitation (~ 5 J cm^{-2}) [145]. Hence, it is unlikely that laser ablation plays a role. Previous studies have reported a reduction of the surface roughness of GaN upon excitation with UV ns laser pulses [146, 147], which could explain the change in SE yield. The change in SE contrast could also be due to increased contamination on the optically-excited surface, similar to the contamination typically observed in SEMs in the electron-irradiated areas [148, 149]. Further experiments with varying laser power, repetition rate and exposure time could be performed to elucidate the origin of this effect.

We further analyze the shape of the laser spot by taking horizontal (x) and vertical (y) cross-sections of the SE image, as shown in Fig. 3.8b and c, respectively. In each case, the curve is obtained by integrating over the rectangle delimited by
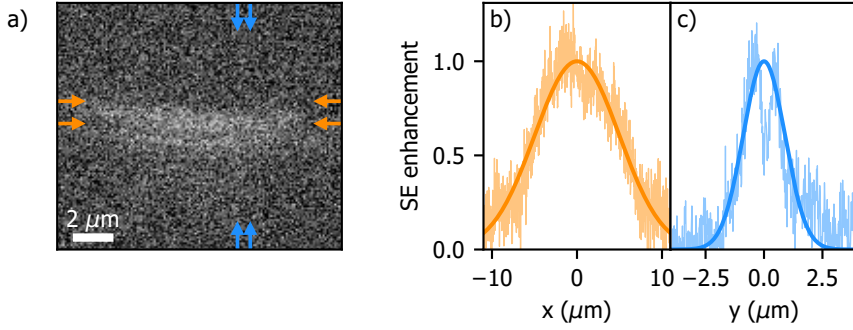
Figure 3.8: Visualization of the laser spot on the sample. (a) SE image of a GaN substrate obtained after excitation with the 3rd harmonic laser beam. Horizontal (b) and vertical (c) cross-sections of the SE image together with the corresponding Gaussian fits, from which we obtain a laser spot size of 11.7 and 2.1 μm in the horizontal and vertical direction, respectively.

the corresponding arrows (orange and blue in Fig. 3.8a). The position of this rectangle is chosen in both cases such that it yields the largest spread, thus ensuring that we characterize the largest section of the laser spot. In this experiment we ensured that the laser power was low enough to avoid any saturation effect. The solid lines represent Gaussian fits, from which we derive a laser spot size (full width at half maximum) of 11.7 and 2.1 μm in the horizontal and vertical directions, respectively. We attribute the asymmetry of the laser spot to non-perfect alignment of the laser beam with respect to the parabolic mirror.

3.5.2. LASER ALIGNMENT ON THE SAMPLE

As shown above, imaging the change in SE yield after laser excitation allows us to characterize the shape and size of the laser spot on the sample. However, we have only observed this effect on specific samples and under excitation with the 3rd harmonic laser beam. Hence, it is not practical for alignment in regular pump-probe experiments. Instead, we can align the laser beam on the sample by analyzing the image on the CCD of the PL beam, similar to the method used to align the parabolic mirror and sample height with CL (section 3.4.1).

We define good alignment of the laser beam as when it is centered with respect to the electron beam, that is, when it is at the focal point of the parabolic mirror. Figures 3.9(b-h) show various images of PL emission from GaN upon laser excitation (3rd harmonic beam, $\lambda = 345$ nm), together with the corresponding SE image of the laser spot on the sample, obtained using the method discussed above. Panel (b) shows an example of satisfactory alignment of the laser. Here the CCD image resembles the one expected for a collimated beam from an off-axis parabolic mirror, as shown in Fig. 3.4, and we observe that the laser spot is centered with respect to the electron beam. The rest of panels in Fig. 3.9 show the CCD pattern and SE
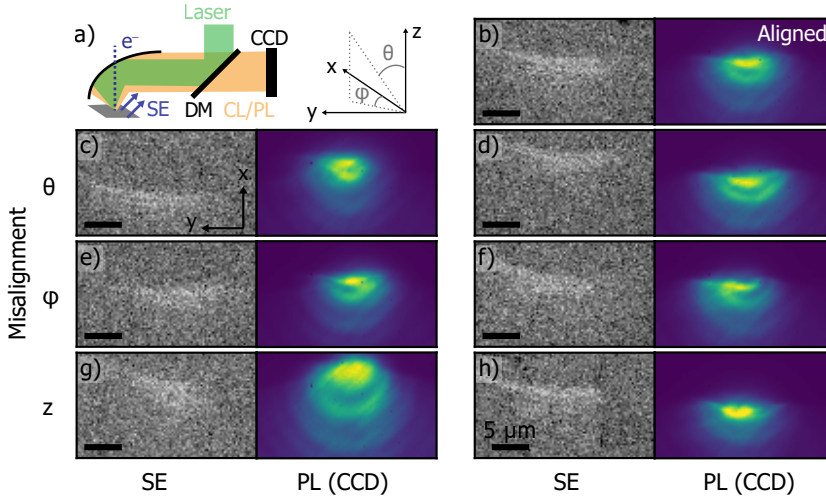
Figure 3.9: Laser alignment on the sample. (a) Left: schematic of the experiment, including PL collection on the CCD camera and secondary electron (SE) image formation. The position of the laser on the sample is tuned by moving the dichroic mirror (or beam splitter) (DM). Right: system of coordinates. (b-h) SE images of the GaN surface after excitation with the 3$^{\text{rd}}$ harmonic laser beam (left) together with the corresponding PL pattern on the CCD (right) for an aligned laser beam (b) and misalignments in the polar (θ) (c,d) and azimuthal (ϕ) (e,f) directions, as well as in the sample height (g,h).

image for different types of misalignments of the incoming angle of the laser (polar, θ, and azimuthal, ϕ, angles) (c-f) and height of the sample (g, h). As a reference, a schematic of the experiment and the coordinate system is shown in Fig. 3.9a. The angle of the laser with respect to the parabolic mirror is tuned by controlling the tilt of the dichroic mirror (DM). We observe a clear correlation of the misalignment of the laser spot with respect to the electron beam and the pattern on the CCD. This shows that we can rely on the alignment of the laser using this technique, instead of having to image the laser spot, as in the previous section.

We should note that the height of the sample is fixed through the CL alignment, corresponding to the optimum collection of CL. This alignment should also correspond to best focus of the laser for a perfectly-collimated laser beam. Imperfections in the collimation can result in a focal point slightly different than the one for CL collection.

3.6. TEMPORAL ALIGNMENT

Pump-probe experiments require precise control of the timing between pump and probe (electron and laser, or vice versa). Here we describe the temporal alignment of the laser and electron pulses. We record the decay statistics of PL and CL separately using the TCSPC setup (see 3.4.3), from which we obtain the difference in arrival time between electron and laser pulses on the sample. Figure 3.10
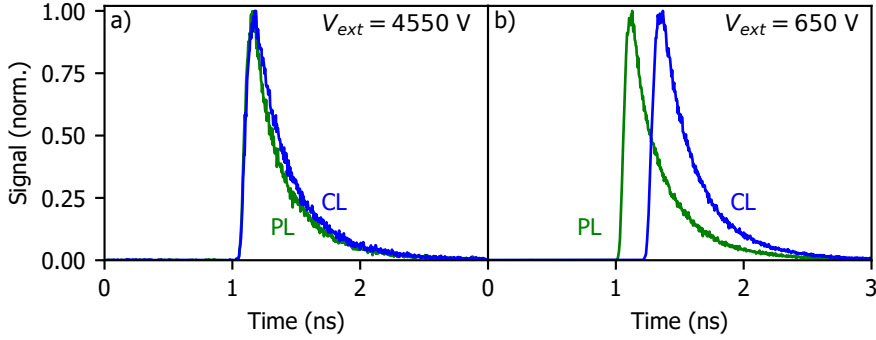
Figure 3.10: Temporal alignment of electron and light pulses. (a) PL (green) and CL (blue) decay traces from GaAs showing a good temporal overlap between electron and light pulses exciting the sample. (b) Same as in (a) but after lowering the extractor voltage, which results in a change in the arrival time of electrons.

shows decay traces of GaAs bandgap emission upon excitation with the laser beam ($\lambda_{\mathrm{exc}} = 345\,\mathrm{nm}$, ~ 5 mW) (green curve) and 30 keV electron pulses (~ 15 electrons per pulse) (blue curve). The extractor voltage at the electron gun was set to 4550 V. The x-axis indicates the time at which photons are detected on the SPAD with respect to the trigger signal. The temporal overlap of both traces, shown in Fig. 3.10a, indicates a good time alignment between electron and laser pulses. The accuracy of this method for determining the zero-delay is limited by the minimum bin size of the time-correlator (4 ps) and uncertainty in the determination of the arrival time of electrons or light from the decay curves. The latter becomes more complex when PL and CL exhibit different decay dynamics. Hence, we typically achieve an accuracy of ~ 10 ps. A higher accuracy in the determination of the zero-delay between electron and laser pulses can be obtained directly through a pump-probe experiment. In that case, the precision of the delay line stages creates an error of ~ 8 fs (see section 3.3), hence the temporal resolution is only limited by the electron (~ ps) and laser (~ 250 fs) pulse duration.

We should note that small changes in the electron or light path directly impact the temporal alignment. As we discussed previously, changing the energy of the electrons from 5 to 30 keV results in a delay of 7.5 ns (section 3.3). The conditions in the photoemission of electrons, discussed in Chapter 2, also determine the arrival time of the electrons. Figure 3.10b shows decay traces of GaAs obtained under the same conditions as in (a) but at low extractor voltage ($V_{\mathrm{ext}} = 650\,\mathrm{V}$). We observe that the CL is now delayed by ~ 200 ps with respect to the PL, which is attributed to the different speed at which electrons travel along the extractor plate. Hence, a precise temporal alignment is essential before starting a pump-probe experiment. Such accurate measurements of the timing of electron arrival can give further insights in electron dynamics in both the electron source and column, both in SEM and TEM.

3.7. COMPARISON BETWEEN CL AND PL

Until now we have focused on the technical aspects of our pump-probe CL setup, including its characterization and different analysis techniques. Here we describe further considerations that are important to take into account when performing a pump-probe experiment, related to the difference between electron and light excitation. PL and (incoherent) CL are often considered as two analogous methods to study the optical properties of materials. They both rely on the spontaneous emission of photons after excitation of a material with either a laser (PL), or high-energy electrons (CL). However, there are significant differences between both types of excitations. In this section we discuss the differences in excitation volume, deposited energy density, spectral emission, quantum efficiency and carrier dynamics in both PL and CL experiments. We illustrate these differences with calculations and experiments on bulk GaAs and GaN samples. All of the experiments are taken in our PP-CL setup, which allows us to excite the same spot on the sample and use the same collection system for both CL and PL emission. Even though each sample studied in PP-CL will require a specific analysis, these results allow us to evaluate the main trends and key parameters for pump-probe experiments.

3.7.1. EXCITATION VOLUME AND ENERGY DENSITY

One of the main discrepancies between electron and laser excitations is the initial excitation volume. In the case of laser excitation, the beam size typically ranges from hundreds of nm to several μm (see section 3.5.1). The penetration depth of the laser light in the sample is determined by the absorption coefficient of each specific material at the excitation wavelength. In contrast, electron beams typically exhibit much smaller spot sizes, from a few nm for a continuous beam to a few hundreds of nm for a pulsed beam, as explained in chapter 2. The primary electron beam travels through the material while suffering inelastic collisions, until it loses all of its energy. The excitation depth, and thus interaction volume, is highly dependent on the initial electron energy.

The difference in excitation volume in PL and CL is illustrated in Figure 3.11. The figure shows calculated maps of the deposited energy density in GaAs for 5 and 30 keV electron beams (a,b) and laser excitation with a wavelength of 345 and 517 nm (c,d, corresponding to the 3rd and 2nd harmonics of our laser). The CL maps are derived from the results of Monte Carlo simulations of the electron trajectory inside the sample, performed using the Casino software [1]. We have assumed an electron beam radius of 20 nm, which is an intermediate between our SEM resolution using continuous and pulsed electron beams. The PL maps are calculated assuming an initial symmetrical Gaussian laser spot with $\sigma = 3\,\mu$m and absorption profile derived using the Beer-Lambert law. The optical parameters of GaAs are extracted from ref. [150].

In all cases we assume a total deposited energy of 100 fJ, which would correspond to an average of ~ 120 electrons per pulse in the case of 5 keV and ~ 20 electrons per pulse for 30 keV. This corresponds to an electron current of 96 and 16 pA, respectively, and laser power of 0.5 μW (at 5 MHz). The color scale in each map is set
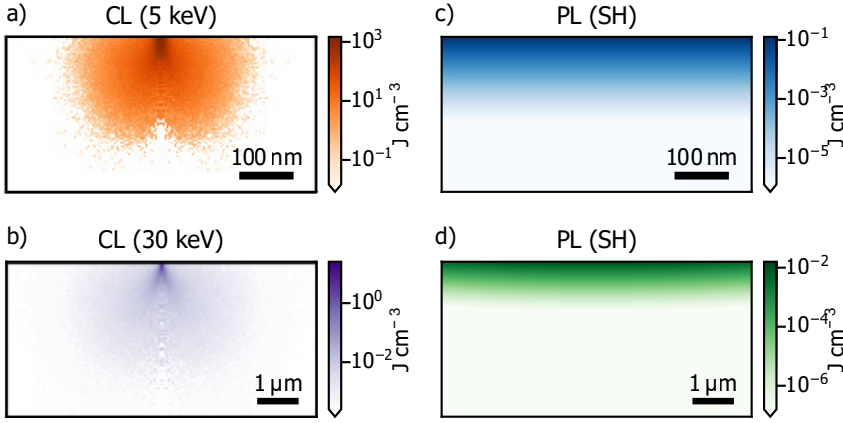
Figure 3.11: PL and CL deposited energy density volume in GaAs. (a) Calculated density of energy deposited on a GaAs sample by 5 keV electrons. (b) Same as in (a) but for electrons with initial energy of 30 keV, showing an increase in the interaction volume and decrease in the energy density with respect to the 5 keV electrons. (c) Deposited energy density after optical excitation with the 3rd harmonic beam for a Gaussian laser spot with $\sigma = 3\,\mu m$. (d) Same as in (c) but for the 2nd harmonic laser beam. In all four cases the total deposited energy corresponds to 100 fJ.

such that it covers 5 orders of magnitude with respect to the highest energy density.

Excitation with 5 keV electrons yields the largest energy density, corresponding to $\sim 10^3\,\mathrm{J\,cm^{-3}}$, due to the small excitation volume. Instead, at 30 keV the maximum energy density decreases by two orders of magnitude, down to $\sim 20\,\mathrm{J\,cm^{-3}}$, given the larger volume excited by the electron. The PL maps exhibit lower densities, ~ 0.1 and $0.01\,\mathrm{J\,cm^{-3}}$ for the 3rd and 2nd harmonic, respectively. Even though the penetration depth is close to that for CL, the larger size of the laser spot on the sample compared to the electron spot results in these lower densities.

To further compare the penetration depth of electrons and light, Figure 3.12 shows the characteristic energy deposition depth in CL as a function of the initial electron energy for GaAs (a) and GaN (b). This length represents the distance from the surface at which the energy of the electron has decreased by $1/e$ on average. In both materials the penetration depth goes from less than 10 nm for a 1 keV electron to more than 1 μm at 30 keV. The plot also shows the absorption length of the 2nd and 3rd harmonic laser beams for the two materials (horizontal lines). The optical data for GaAs and GaN are obtained from refs. [150] and [151], respectively. In GaAs the 3rd harmonic barely penetrates inside the material due to its large extinction coefficient, while the 2nd harmonic beam reaches a depth of $\sim 100\,\mathrm{nm}$, matching the energy deposition depth for electrons between 5 and 10 keV. In the case of GaN, the absorption length of the 3rd harmonic matches the ones for 5-10 keV electrons ($\sim 100\,\mathrm{nm}$). Data for the 2nd harmonic is not shown given that the photon energy is below the GaN band gap ($\sim 365\,\mathrm{nm}$). This analysis shows that in pump-probe
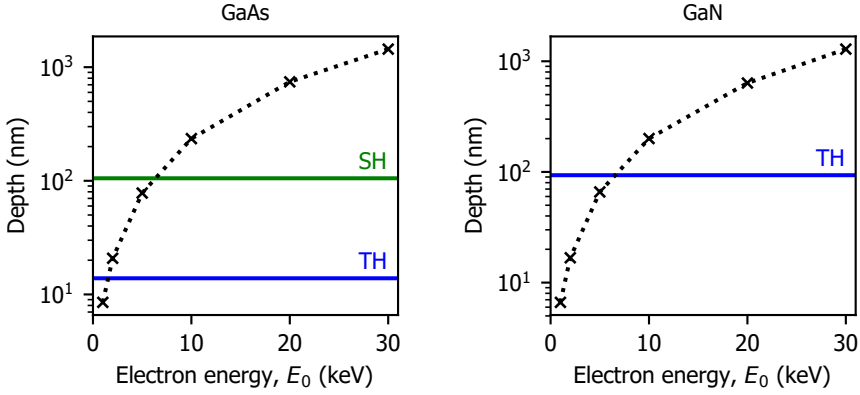
Figure 3.12: Electron and light absorption length in GaAs and GaN. (a) Calculated $1/e$ depth of energy deposition of an electron inside GaAs as a function of its initial energy, extracted from Monte Carlo simulations using the Casino software [1]. The horizontal lines correspond to the optical absorption length for λ_{exc} = 345 and 517 nm (blue and green, corresponding to the 3rd and 2nd harmonic beams). (b) Same as in (a) but for a GaN sample.

experiments it is important to consider the overlap of electron and laser excitations inside the material, in addition to the spatial and temporal alignment discussed above (sections 3.5 and 3.6).

3.7.2. SPECTRAL EMISSION

In our PP-CL setup we can acquire PL and CL spectra on the same area on the sample, thus enabling a direct comparison between both spectral emissions. Figure 3.13a shows CL spectra obtained on an undoped GaAs sample (Nanografi, $350 \pm 25\,\mu$m-thick) at different electron excitation energies (1 to 30 keV, curves from purple to yellow, respectively). The spectra were obtained using a continuous electron beam with electron current in the 400-900 pA range. The spectra exhibit a dominant peak around 860 nm, which matches with the band gap of GaAs at 300 K [152]. The spectra also show an additional peak around 1000 nm, which has been previously attributed to Ga vacancy defects [153, 154]. We observe that the band gap emission redshifts by around 7 nm with increasing electron energy. Redshift of band gap emission is frequently observed in GaAs for increasing temperature [152, 155], due to temperature-dependent band gap energy [156–158]. This suggests that higher electron energies induce a larger heating of the lattice, similar to the redshift observed on GaN nanowires for increasing electron current [159]. This redshift could also be related to differences in material quality along the depth of the sample, given that more energetic electrons probe deeper regions (see Fig. 3.13a). However, PL spectra using the 2nd and 3rd harmonics do not show this effect despite their different absorption depths (Fig. 3.12a), as will be seen below, thus discarding this hypothesis. Other effects, such as saturation of shallow defects, typically result
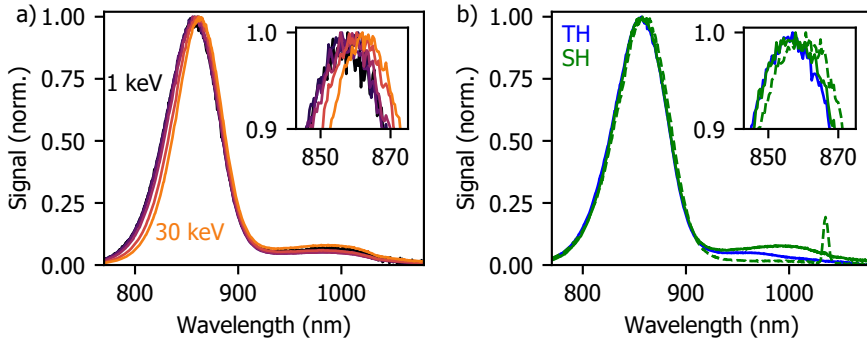
Figure 3.13: PL and CL spectra of GaAs. (a) CL spectra of a GaAs sample after excitation with a continuous electron beam with energy from 1 up to 30 keV (black to orange) (400-900 pA). The spectra exhibits a redshift with increasing electron energy. (b) PL spectrum on GaAs obtained after excitation with the 2nd ($\lambda_{exc} = 517$ nm) and 3rd ($\lambda_{exc} = 345$ nm) harmonics of the laser (solid green and blue curves, 33 and 2 μW, respectively). The plot also shows a measurement obtained at higher excitation power (2.5 mW, 2nd harmonic, dashed green curve), which also exhibits a redshift.

in a blueshift of the spectra [160], and are thus unlikely.

Figure 3.13b shows PL spectra obtained upon excitation with the 3rd harmonic (blue curve, 33 μW) and the 2nd harmonic (solid green curve, 2 μW). Both spectra exhibit a peak at around 856 nm, similar to the CL curves at low electron energy. However, exciting the sample with a larger laser power (2.5 mW, 2nd harmonic) also results in a ∼ 4 nm redshift, as shown in Fig. 3.13b (dashed green curve), thus further suggesting that it is related to heating of the sample. The sharp peak at 1035 nm observed in this curve corresponds to the 2nd order of the spectrometer grating for the excitation wavelength ($\lambda_{exc} = 517$ nm).

CL measurements on an undoped n-type GaN sample (PI-KEM, 30 μm-thick GaN on sapphire) also exhibit a small redshift (∼ 2 nm) in the emission wavelength for increasing electron energy, as shown in Figure 3.14a (200 − 500 pA electron current). In this case, the spectra are centered around the band gap energy of GaN (∼ 365 nm at 300 K [161]), and the redshift could also be attributed to an increase of lattice temperature, as previously reported [159, 161]. However, in this case the emission is composed of contributions from different peaks in the 360 − 370 nm spectral range. The contributions are more clearly visible in the PL spectrum obtained upon excitation with the 3rd harmonic laser beam (3 μW), as shown in Fig. 3.14b. Here we observe two peaks centered at 362 and 368 nm, as well as a broader and weaker peak around 380 nm. The presence of several spectral lines in GaN luminescence has been previously reported and is attributed to different defect-induced luminescence transitions [162]. Hence, the change in spectra observed in this case could also be attributed to differences in the contributions of the individual peaks for different electron energies. Given the different penetration depth of at varying electron energies, differences in defect concentration along the depth of
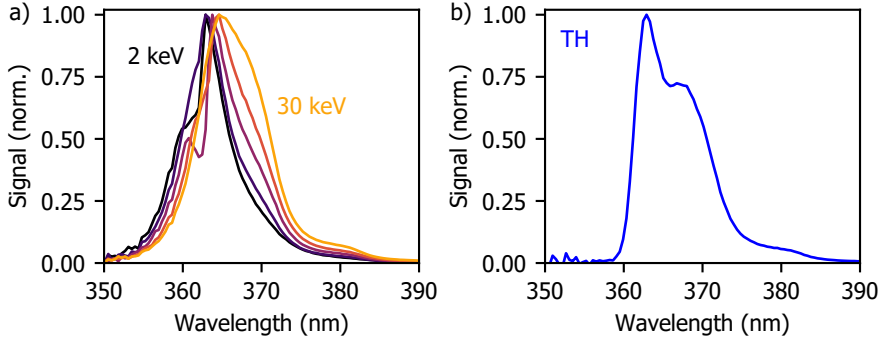
Figure 3.14: PL and CL spectra of GaN. (a) CL spectra of a GaN sample upon excitation with a continuous electron beam with energy from 2 up to 30 keV (black to orange) (200 – 500 pA). The spectra exhibits a redshift with increasing electron energy. (b) PL spectrum on GaN obtained after excitation with the 3rd harmonic laser beam ($\lambda_{exc} = 345$ nm, 3 µW).

the sample could play a role. Further CL studies at low temperature, as well as comparison between samples with varying crystal quality, are needed to better understand the role of electron energy on the CL spectra. We should note that in our samples, the contribution of yellow-band emission, typically in the 500-700 nm spectral range [163], is negligible compared to emission around the band gap energy.

3.7.3. QUANTUM EFFICIENCY
In the previous section we have analyzed the difference between PL and CL in a qualitative way, by investigating the differences in emission spectra. Next, we compare quantitatively the PL and CL band gap emission in GaAs and GaN. To do so, we define a common figure of merit: the quantum efficiency (QE), that is,

$$QE = \frac{N_{emitted}}{N_{carr}} \tag{3.2}$$

where $N_{emitted}$ is the number of photons emitted in the sample and N_{carr} refers to the maximum number of charge carriers generated after excitation with either electrons or light.

PL QUANTUM EFFICIENCY
In PL, absorption of a photon with energy larger than the band gap results in the excitation of an electron from the valence to the conduction band. The generated charge carrier thermalizes to lower energy states in the conduction band before recombining, either radiatively or non-radiatively. Hence, the maximum number of generated carriers directly corresponds to the number of absorbed photons, that is, $N_{carr} = (1 - R)P_0 T \frac{\lambda_{exc}}{hc}$. Here, R is the reflectance of the material at the excitation wavelength λ_{exc}, P_0 is the incident power, T is the exposure time, h is Planck's constant and c is the speed of light.

To calculate the number of emitted photons (N_{emitted}), defined as number of radiative recombination events, from the signal detected on the spectrometer, we need to account for several loss factors in the luminescence collection. First, we account for reabsorption of the emitted photons. This loss factor (η_{reabs}) is calculated by applying Beer-Lambert's law on the initial absorption profile (see map of absorbed energy in Fig. 3.11c,d). We assume that re-emission of the reabsorbed photons is negligible, which is reasonable given the low quantum efficiencies obtained (as will be discussed below). Second, only photons emitted within the critical angle of the material can escape the sample. Assuming isotropic emission inside the material, the escape efficiency becomes $\eta_{\text{esc}} = 1 - \cos\theta_c$, where θ_c is the critical angle of the material. Third, we account for the mismatch between the laser spot size ($\sim 11\,\mu\text{m} \times 2\,\mu\text{m}$, section 3.5.1) and collection area of the parabolic mirror ($\sim 10\,\mu\text{m} \times 10\,\mu\text{m}$), meaning that not all photons emitted from the sample are collected. Taking into account the collection area of our mirror and the dimensions of our laser spot, we calculate this loss factor to be $\eta_{\text{spot}} \approx 0.7$. Finally, the collection efficiency of the rest of the optical system is accounted for using the calibration obtained from transition radiation (TR), as described in section 3.4.2. However, we need to correct for the fact that TR exhibits a toroidal angular emission pattern [26, 32], in contrast to the Lambertian pattern typically observed for semiconductors [26]. Taking into account the geometry of our parabolic mirror, the collection efficiency is $\eta_{\text{TR}} = 0.82$ for TR and $\eta_{\text{Lamb}} = 0.86$ for Lambertian emission [41]. Hence, we can express the quantum efficiency in PL as

$$QE_{\text{PL}} = \frac{hc}{(1-R)P_0 T\lambda_{\text{exc}}} \frac{\eta_{\text{Lamb}}}{\eta_{\text{TR}}\eta_{\text{esc}}\eta_{\text{reabs}}\eta_{\text{spot}}} \int_{\lambda_1}^{\lambda_2} \frac{S(\lambda)}{\eta_{\text{coll}}(\lambda)}\, d\lambda. \tag{3.3}$$

Here, $S(\lambda)$ is the acquired spectrum, in units of counts per spectral bandwidth, and $\eta_{\text{coll}}(\lambda)$ is the collection efficiency of the system (Fig. 3.5b). The limits of the integral, λ_1 and λ_2, are taken such that they include the entire PL emission spectrum.

CL QUANTUM EFFICIENCY

The excitation process in CL is fundamentally different from the PL case. After entering a material, the primary electron, with energy E_0, deposits energy in the sample through inelastic collisions. One of the dominant interactions of high energy electrons with a material is the generation of bulk plasmons (also referred to as volume plasmons), defined as the collective oscillation of valence electrons [13, 28, 29]. The energy of a bulk plasmon (E_{plasmon}), typically $10-30\,\text{eV}$, is determined by the density of valence electrons of the material [13], and is thus characteristic for each material. The excited bulk plasmons decay through the excitation of high-energy carriers, which thermalize to the lower states of the conduction band by generating carriers with lower energy, phonons and secondary electrons [28, 164, 165].

We then define the maximum number of thermalized carriers, with energy E_{BG}, generated in CL as

$$N_{\text{carr}} = N_p N_{c,p} \frac{IT}{q} \approx (1-\Gamma)\frac{E_0}{E_{\text{BG}}}\frac{IT}{q} \tag{3.4}$$

where Γ is the fraction of back-scattered electrons, I is the electron current, T is the acquisition time and q is the electron charge. $N_{\mathrm{p}} = E_0/E_{\mathrm{plasmon}}$ is the maximum number of plasmons created per electron, and $N_{c,p} = E_{\mathrm{plasmon}}/E_{\mathrm{BG}}$ is the maximum number of thermalized carriers created per plasmon. The approximate sign in the last equality of Eq. 3.4 represents the fact that in practice the number of carriers (N_p and $N_{c,p}$) is an integer, which is taken into account in the calculations.

In order to calculate the number of emitted photons (N_{emitted}) we consider the same losses as in the PL case, except for the loss related to the mismatch between the laser spot and collection area of the mirror (η_{spot}). In CL, the excitation of electrons is very localized, and thus all photons are efficiently collected by the parabolic mirror. The expression for the quantum efficiency in CL is

$$QE_{\mathrm{CL}} = \frac{E_{\mathrm{BG}}}{(1-\Gamma)E_0} \frac{q}{IT} \frac{\eta_{\mathrm{Lamb}}}{\eta_{\mathrm{TR}}\eta_{\mathrm{esc}}\eta_{\mathrm{reabs}}\eta_{\mathrm{spot}}} \int_{\lambda_1}^{\lambda_2} \frac{S(\lambda)}{\eta_{\mathrm{coll}}(\lambda)} \, d\lambda \,, \qquad (3.5)$$

with $S(\lambda)$ the CL spectrum in units of counts per spectral bandwidth.

We should note that the method and model presented here to calculate PL and CL quantum efficiencies might result in less accurate results than conventional techniques, such as PL quantum yield quantification [166] or direct EQE measurements. This lower accuracy is due to the error in the quantification of the spectra ($\sim 30\%$, as discussed in section 3.4.2). However, it enables direct comparison of PL and CL efficiencies at the same conditions and on the same area on the sample, which is critical to study the differences between electron and light excitation.

EXPERIMENTAL CL/PL QUANTUM EFFICIENCY

Figure 3.15 shows the CL quantum efficiency obtained for GaAs (a) and GaN (b) samples as a function of electron energy, extracted from the data presented in Figs. 3.13 and 3.14, respectively. We observe quantum efficiencies in the $10^{-4} - 10^{-2}$ range for GaAs and in the $10^{-4} - 10^{-3}$ range for GaN, which is reasonable considering reported values in literature [167, 168]. The quantum efficiency exhibits an increase with increasing electron energy in both GaAs and GaN of more than 1 order of magnitude. We hypothesize that this enhancement is due to the effect of surface recombination, as previously proposed in CL studies of GaN [169]. Surface recombination is known to impact the quantum efficiency in both GaAs and GaN [167, 170]. Electrons with larger energies penetrate deeper inside the material, as discussed above (section 3.7.1), thus creating carriers that are further away from the surface.

The PL quantum efficiency is also plotted in Fig. 3.15 for both GaAs and GaN (a and b) upon excitation with the 2$^{\mathrm{nd}}$ and 3$^{\mathrm{rd}}$ harmonic of the laser (green and blue horizontal lines, respectively). In GaAs, the extracted quantum efficiency is higher when exciting with the 2$^{\mathrm{nd}}$ harmonic compared to excitation with the 3$^{\mathrm{rd}}$ harmonic ($\sim 10^{-4}$ and 10^{-3}, respectively). Given the larger absorption depth when using the 2$^{\mathrm{nd}}$ harmonic beam (Fig. 3.12), these results match with the hypothesis that surface recombination is the mechanism responsible for the increase in quantum efficiency with increasing electron energy.
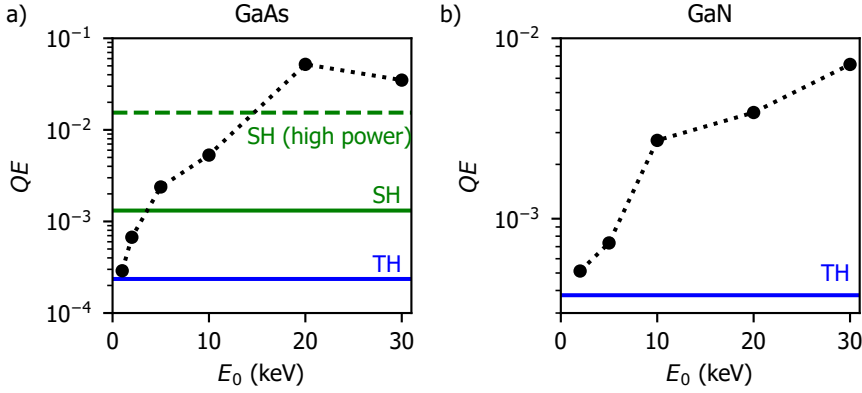
Figure 3.15: PL and CL quantum efficiency of GaAs and GaN. (a) CL quantum efficiency for GaAs extracted from the experiments shown in Fig. 3.13 and calculated using Eq. 3.5 for different electron energies, together with the PL quantum efficiencies (Eq. 3.3) for excitation with the 2nd and 3rd harmonic laser beams (green and blue horizontal lines). (b) Same as in (a) but for GaN (data from Fig. 3.14).

An additional explanation could be that the increase in quantum efficiency is related to the redshift in the emission spectra observed for both GaAs and GaN (Figs. 3.13 and 3.14). However, heating of the lattice, which produces a redshift, typically results in lower quantum efficiencies [155, 171, 172]. Hence, it is less likely that these effects are correlated, and the decrease of efficiency due to temperature might be weaker than the enhancement due to reduced surface recombination.

Finally, we found that the PL quantum efficiency upon excitation with the 2nd harmonic at high power (2.5 mW, same as in Fig. 3.13b) is also larger than at lower power (2.0 μW, solid lines in Fig. 3.15). A possible explanation for this could be saturation of non-radiative traps, either surface or bulk defects, thus leading to an improved quantum efficiency.

These results show that electron and laser excitation can result in different quantum efficiencies, which should be taken into account when performing PP-CL measurements. To fully elucidate the mechanisms behind the increase the changes in CL quantum efficiency we should perform further experiments, such as a systematic comparison of passivated samples, which are beyond the scope of this section. The method presented here to extract PL and CL quantum efficiencies offers a way to perform quantitative studies of both luminescence mechanisms.

3.7.4. CARRIER DYNAMICS

Finally, our PP-CL setup also allows us to study both PL and CL temporal decays. Here we perform time-resolved measurements on GaAs using the TCSPC setup discussed in section 3.4.3. Figure 3.16 shows CL decay traces obtained when exciting with 10 and 30 keV electron pulses (a and b, respectively) for different number of electrons per pulse. The number of electrons per pulse ranges from 2 up to ~ 720
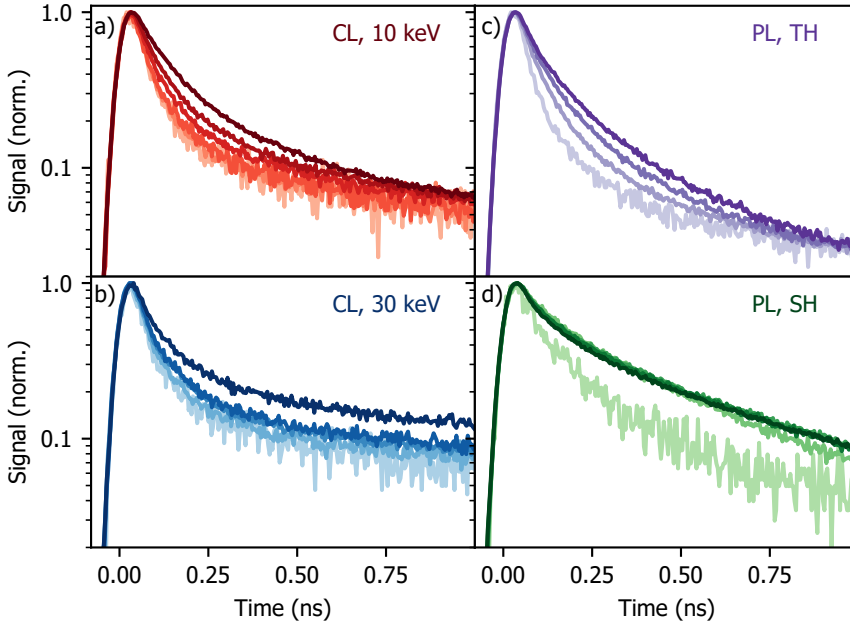
Figure 3.16: Decay dynamics in GaAs. (a) CL time traces obtained upon excitation with a pulsed electron beam (10 keV) containing an average of 2, 30, 110, 250, 380 and 720 electrons per pulse (light to dark orange). (b) Same as in (a) but for a 30 keV beam, with 0.4, 6, 30, 60 and 190 electrons per pulse (light to dark blue). (c) PL time traces obtained after laser excitation (3rd harmonic, $\lambda_{exc} = 345\,nm$) for increasing energy per pulse (3, 46, 113 and 211 pJ, light to dark purple). (d) Same as in (c) but for excitation with the 2nd harmonic ($\lambda_{exc} = 517\,nm$,) (4, 105, 232, 334 and 498 pJ, light to dark green).

in the case of 10 keV (light to dark red curves), and from less than 1 to ∼ 180 for 30 keV (light to dark blue curves). The experiments were done using an extractor voltage of 650 V. We also performed PL experiments obtained when exciting the sample with the 3rd and 2nd harmonics of the laser (c and d, respectively), and for increasing energy per pulse (from ∼ 3 up to ∼ 500 pJ), using a laser repetition rate of 5.04 MHz. In all cases we observe a dominant fast decay in the $100 - 200\,ps$ regime. Interestingly, both CL and PL signals exhibit slower decays for increasing fluence, either electrons or photons. This observation is in contrast with the trends expected when only bimolecular or Auger processes dominate the recombination processes. In those cases, an increase in the initial carrier density leads to a faster decay of the signal [172, 173].

To further explore this effect, in Figure 3.17 we plot the characteristic $1/e$ time (τ_c) as a function of the deposited energy per pulse, for both CL (a) and PL (b). The CL data shows a linear increase of τ_c from ∼ 100 up to ∼ 180 ps. The trends for 10 and 30 keV electrons are very similar, despite the difference in energy density (which is directly related to carrier density) expected for different electron energies
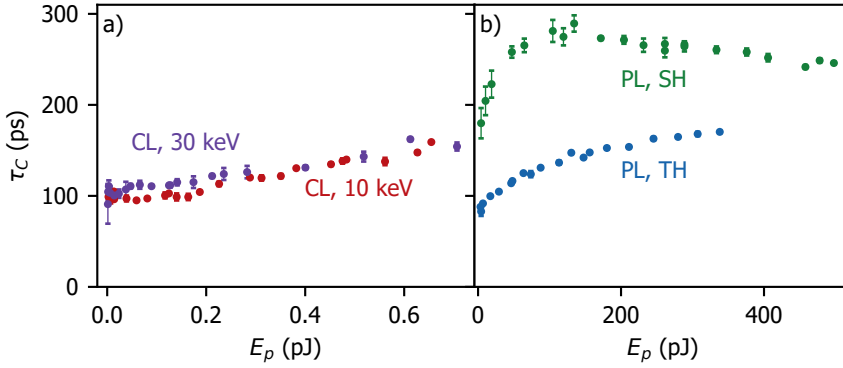
Figure 3.17: PL and CL decay times vs. injected energy. (a) Characteristic time (τ_c) in CL as a function of the deposited energy per pulse for 10 and 30 keV electron beams. (b) Same as in (a) but for PL obtained upon laser excitation with the 2nd and 3rd harmonics.

(see section 3.7.1). This observation also suggests that bimolecular and Auger recombination are not the dominant decay mechanisms, since they directly depend on carrier density.

In the case of PL, we observe a difference between excitation with the 2nd or 3rd harmonic laser beams. Irradiation with the 3rd harmonic results in a characteristic time increasing from ∼ 80 to ∼ 160 ps for increasing deposited energy, which is in a similar range as the decay times found in CL. In this case the trend is sub-linear, and shows a gradual saturation for increasing energy per pulse. Instead, when using the 2nd harmonic beam we obtain larger τ_c. We observe an increasing trend from ∼ 180 to ∼ 280 ps, up to an energy per pulse of ∼ 90 pJ, above which the decay time slightly decreases to ∼ 240 ps.

An increase in decay time for larger injected carrier densities has been previously observed and attributed to saturation of defect states [174–177]. At low injection levels, carriers have a high probability of being trapped. Instead, at higher injection levels, an increasing number of defects is occupied, thus effectively reducing the recombination rate of carriers. This hypothesis should be validated with further experiments and modelling. Time-resolved experiments at low temperature could help to evaluate the contribution of defects states to the observed decay times. Moreover, a complete decay rate model including the different recombination paths should be developed for a full understanding of carrier dynamics in GaAs.

Overall, the comparison between CL and PL excitation volumes, deposited energy densities, spectra, quantum efficiency and carrier dynamics provides insights into the differences between electron and light excitation of semiconductors, which should be accounted for in PP-CL experiments.
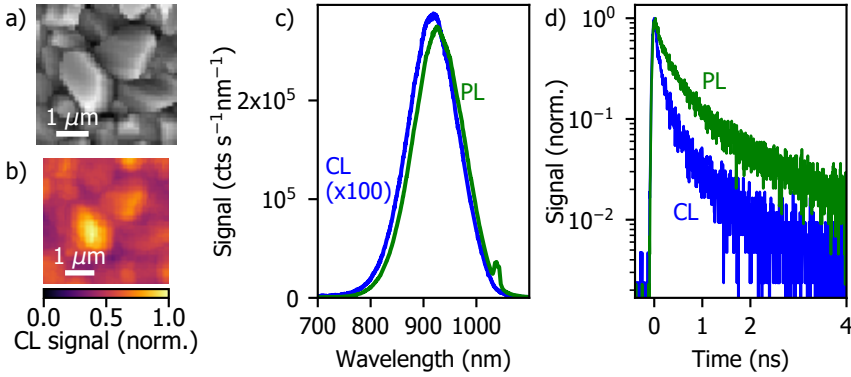
Figure 3.18: CL and PL measurements on CZTS. (a) SE image of a CZTS sample together with the corresponding CL map (b), showing the CL signal integrated over a 600 − 1000 nm wavelength range. (c) PL (green) spectrum obtained upon excitation with the 2ndd harmonic laser beam, together with the CL spectrum (blue) obtained when using a 10 keV pulsed electron beam. The CL signal is a factor 100 lower than the PL signal. (d) PL (green) and CL (blue) decay traces obtained under the same conditions as (c).

3.8. EXAMPLE OF A PP-CL MEASUREMENT

Finally, we discuss the procedure and analysis of a complete PP-CL experiment. The PP-CL setup enables two possible configurations, with the electron acting either a pump or a probe. A full study of a PP-CL experiment in which the electron acts as a pump is presented in Chapter 4. Here, we describe the first results obtained using the second configuration of the setup, in which the electron acts as a probe.

We perform our study on a Cu_2ZnSnS_4 (CZTS) sample, which was fabricated by the group of Prof. X. Hao at the University of New South Wales (Sydney). The sample consists of a ∼ 800 nm-thick CZTS layer deposited on top of a Mo/glass substrate. A ∼ 3 nm layer of Al_2O_3 is deposited on top for passivation. CZTS is a promising new photovoltaic material, based on fully earth-abundant materials, and thus knowledge of its carrier recombination dynamics is important for further use in solar cells [178, 179].

Figure 3.18a shows a SE image of the sample obtained with a 10 keV continuous electron beam (∼ 154 pA), from which we observe the different grain boundaries. We also show a CL map acquired simultaneously (Fig. 3.18b). The CL colormap represents the normalized CL signal integrated over the entire wavelength range, thus showing the dependence of CL emission on the position on the sample. The CL map reflects the position of the grain boundaries, with the darker regions corresponding to the edges of the grains. This spatial dependence of the CL intensity could be due to non-radiative carrier recombination near the grain edges, as well as differences in electron excitation efficiency and CL escape probability. A more detailed analysis is necessary, such as a $g^{(2)}(\tau)$ analysis, as discussed in Chapter 5,

from which we can extract the electron excitation efficiency.

CL and PL spectra of the sample are shown in Fig. 3.18c. The PL spectrum was obtained when exciting the sample with the 2nd harmonic laser beam ($\lambda = 517$ nm, 25 pJ per pulse at 25.19 MHz). We use a 532 nm long-pass filter in the detection path to suppress the remaining pump light. The CL spectrum was obtained under a 10 keV pulsed electron beam containing 636 ± 33 electrons per pulse. We attribute the uncertainty in the number of electrons per pulse to the the variation of 4th harmonic laser power used to generate electron pulses. Here we used photoemission conditions for high current ($V_{ext} = 650$ V, $C_1 = 540$ V, 1 mm aperture, see Chapter 2), thus resulting in a low spatial resolution. The CL spectrum has been multiplied by a factor 100 for easier comparison to the PL spectrum. The electron and laser beam conditions described here correspond to the ones used in the pump-probe experiments shown below. Both spectra exhibit an emission peak centered around 918 and 926 nm for CL and PL, respectively. These spectra are similar to the ones obtained in other works under optical excitation [160], and are usually attributed to close-to-bandgap emission. The differences in peak wavelength emission between PL and CL could be due to different levels of saturation of shallow tail states in each case. In our sample, we have also observed a change of PL peak emission as a function of laser power, similar to previous studies, which is attributed to saturation of trap states [160]. The small sharp peak around 1035 nm observed in the PL spectrum corresponds to the second-order diffraction of the excitation laser beam from the spectrometer grating. Fig. 3.18d shows PL and CL decay traces obtained using the TCSPC setup, which we used to temporally align the arrival of electron and laser pulses on the sample.

Next, we performed pump-probe experiments. Given the large difference between the CL and PL signals (PL is a factor 100 larger) we used lock-in detection, as described in section 3.4.4. The electron beam was modulated at a frequency of 287 Hz. The output voltage of the MPPC module was below 300 mV when collecting both PL and CL, which is well below the saturation value of the detector at 25.19 MHz (Fig. 3.7c). A PP experiment consists of the acquisition of N sets of measurements, each at a different position of the delay stage, corresponding to a certain delay between electron and light pulses. These N measurements are performed in a random order, such that we can disregard any artificial trends due to sample degradation or drift in the system. At each position of the delay stage we perform one set of measurements, consisting of 2 acquisitions: CL, that is, only electrons exciting the sample, and PP, i.e., laser and electron on the sample. In the CL-only measurement, the light-injection path is mechanically blocked with a software-controlled flip mount, such that the laser beam does not excite the sample. Hence, we acquire only CL emission. We record the average signal read by the lock-in amplifier during the exposure time T_{exp}, and repeat the acquisition n times to improve the statistics. Here we used $T_{exp} = 30$ s and $n = 4$. The CL emission is recorded at every delay position to compensate for effects such as sample degradation or fluctuations in the electron current. Next, the light-injection path is unblocked such that electrons and light excite the sample synchronously, thus producing both CL and PL. The
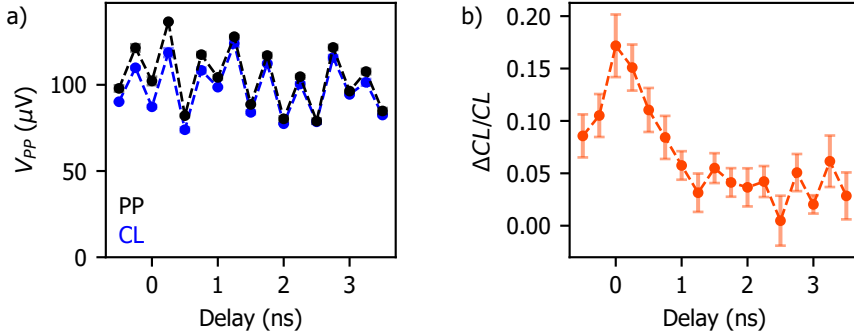
Figure 3.19: Pump-probe measurements on CZTS using a lock-in amplifier. (a) Signal obtained when exciting with only electron pulses (CL, blue) and electron and light pulses (PP, black) at different delays between electrons and light. A positive delay is defined as the arrival of the electron pulse after the light pulse. (b) Normalized CL change as a function of delay. We observe an increase in the CL signal right after optical excitation of the sample, which decreases for increasing delay.

signal is recorded by the lock-in using the same settings as in the CL-only measurement (T_{exp} and n). Hence, a set of measurements at each position of the delay scan takes a time of $2nT_{\text{exp}}$ (here, 4 min). We could add a third measurement of PL-only, such that the laser beam that is focused on the electron cathode (4th harmonic) is blocked. However, the PL background signal read by the lock-in amplifier was negligible ($< 1\,\mu\text{V}$, compared to $\sim 100\,\mu\text{V}$ of CL), thus this was not needed.

The results of a PP experiment on CZTS are shown in Figure 3.19. We used an electron current of $1.28 \pm 0.13\,\text{n}A$ (318 ± 39 electrons per pulse). All other excitation parameters were kept the same as for the spectra and decay traces shown in Fig. 3.19. We scanned the delay line over a range from -0.5 to $3.5\,\text{ns}$ with step size of $\delta t = 0.25\,\text{ns}$. Positive delay is defined as the arrival time of the electron pulse (probe) after the laser pulse (pump). The entire experiment took $\sim 1\,\text{h}$, which was split into two shorter scans of $\sim 30\,\text{min}$ each, scanning from -0.5 to $3.5\,\text{ns}$ with $\delta t = 0.5\,\text{ns}$, and from -0.25 to $3.25\,\text{ns}$, also with $\delta t = 0.5\,\text{ns}$. Long acquisitions can be challenging due to drift of the alignment of the laser beam on the electron cathode, thus decreasing the current on the sample. Hence, splitting an experiment into short scans allows us to perform realignment in between measurements if needed. Moreover, keeping the electron cathode at a low temperature for a long period of time results in a decrease in the emitted current, thus it is desirable to quickly warm up the tip in between measurements (see Chapter 2 for details).

Panel (a) of Fig. 3.19 shows the peak-to-peak voltage read by the lock-in amplifier for CL (blue) and PP (black) at the different positions of the delay stage. The CL signal is around $100\,\mu\text{V}$, with variations of up to 25 %, which we attribute to fluctuations in the power of the laser beam that excited the electron cathode ($\sim 1\,\text{Hz}$). The PP data exhibits similar variations, but its absolute value is systematically larger than the CL one at small delays. To further analyze the pump-probe effect, we di-

vide the change in CL, defined as $\Delta CL = PP - CL - PL$, by the CL signal. A value of zero means that the CL emission is unaffected by the presence of the laser. Instead, in Fig. 3.19b we observe a clear initial enhancement of the CL signal near zero delay. The increase in CL is ~ 17% at zero delay, and decreases for longer pump-probe delay. Similar trends were reproduced on different positions on the CZTS film. The error bars in the figure are calculated from the standard deviations of the CL and PP measurements in panel (a). The mechanism responsible for this CL enhancement is preliminary attributed to the filling of defect states by the laser beam, and the subsequent emptying of these states in the ns timescale. Further measurements and modeling are now ongoing to study these PP-CL transients more in detail, which account for the different carrier recombination rates, including bimolecular recombination, and monomolecular recombination through defect states. These measurements represent the first initial studies of PP-CL using electrons as a probe and with dependence on the delay between electron and light pulses.

3.9. CONCLUSION

In this chapter we have presented the design of a new instrument for pump-probe cathodoluminescence experiments. In the first part of the chapter we have discussed the technical implementation of the setup, based on the coupling of a fs laser to the electron cathode and sample chamber of a Quanta 250 FEG SEM. The setup allows for different types of analysis of the luminescence emitted by the sample (either PL or CL), including spectroscopy, time-resolved and autocorrelation measurements, and lock-in based detection. The spatial overlap of electron and light pulses on the sample is performed by visualizing the laser spot on the sample, or by analyzing the angular emission of the PL light, while the temporal overlap is achieved by monitoring the arrival time of electrons and light through time-resolved PL and CL measurements.

In the second part of the chapter, we discussed some important considerations to take into account when performing pump-probe experiments. We compared electron and light excitation mechanisms in terms of interaction volume, density of deposited energy, emission spectra, quantum efficiency and carrier dynamics. Experimental data on GaN and GaAs show that excitation with increasing electron energy results in a redshift of band gap emission, as well as an increased quantum efficiency compared to PL experiments performed on the same area on the sample. Time-resolved measurements on GaAs show the same trends for both electron and laser excitation. We observe that the characteristic time increases for increasing fluence, which is preliminary attributed to saturation of defect states.

Finally, we presented initial studies of PP-CL measurements on Cu_2ZnSnS_4, in which we used the electron as a probe. We observe that excitation of the sample with the laser results in a transient CL enhancement on the ns timescale. A second configuration of our PP-CL setup is illustrated in the next chapter, in which the electrons act as a pump.